



# Hadron production and propagation in pion-induced reactions on nuclei

HADES collaboration

R. Abou Yassine<sup>6,13</sup>, J. Adamczewski-Musch<sup>5</sup>, O. Arnold<sup>9,10</sup>, E. T. Atomssa<sup>13</sup>, M. Becker<sup>11</sup>, C. Behnke<sup>8</sup>, J. C. Berger-chen<sup>9,10</sup>, A. Blanco<sup>1</sup>, C. Blume<sup>5,8,e</sup>, M. Böhmer<sup>10</sup>, L. Chlad<sup>14,g</sup>, P. Chudoba<sup>14,g</sup>, I. Ciepał<sup>3</sup>, S. Deb<sup>13</sup>, C. Deveaux<sup>11</sup>, D. Dittert<sup>6</sup>, J. Dreyer<sup>7</sup>, E. Epple<sup>9,10</sup>, L. Fabbietti<sup>10</sup>, P. Fonte<sup>1,a</sup>, C. Franco<sup>1</sup>, J. Friese<sup>10</sup>, I. Fröhlich<sup>8</sup>, J. Förtsch<sup>18</sup>, T. Galatyuk<sup>5,6,c</sup>, J. A. Garzón<sup>15</sup>, R. Gernhäuser<sup>10</sup>, R. Greifehagen<sup>7,d,†</sup>, M. Grunwald<sup>17</sup>, M. Gumberidze<sup>5</sup>, S. Harabasz<sup>6,c</sup>, T. Heinz<sup>5</sup>, T. Hennino<sup>13</sup>, C. Höhne<sup>5,11</sup>, F. Hojeij<sup>13</sup>, R. Holzmann<sup>5</sup>, M. Idzik<sup>2</sup>, B. Kämpfer<sup>7,d</sup>, K.-H. Kampert<sup>18</sup>, B. Kardan<sup>8,e</sup>, V. Kedych<sup>6</sup>, I. Koenig<sup>5</sup>, W. Koenig<sup>5</sup>, M. Kohls<sup>8,e</sup>, J. Kolas<sup>17</sup>, B. W. Kolb<sup>5</sup>, G. Korcyl<sup>4</sup>, G. Kornakov<sup>17</sup>, R. Kotte<sup>7</sup>, W. Krueger<sup>6</sup>, A. Kugler<sup>14</sup>, T. Kunz<sup>10</sup>, R. Lalik<sup>4</sup>, K. Lapidus<sup>9,10</sup>, S. Linev<sup>5</sup>, F. Linz<sup>6,5</sup>, L. Lopes<sup>1</sup>, M. Lorenz<sup>8</sup>, T. Mahmoud<sup>11</sup>, L. Maier<sup>10</sup>, A. Malige<sup>4</sup>, J. Markert<sup>5</sup>, S. Maurus<sup>10</sup>, V. Metag<sup>11</sup>, J. Michel<sup>8</sup>, D. M. Mihaylov<sup>9,10</sup>, V. Mikhaylov<sup>14,g</sup>, A. Molenda<sup>2</sup>, C. Müntz<sup>8</sup>, R. Münzer<sup>9,10</sup>, M. Nabroth<sup>8</sup>, L. Naumann<sup>7</sup>, K. Nowakowski<sup>4</sup>, J. Orliński<sup>16</sup>, J. -H. Otto<sup>11</sup>, Y. Parpottas<sup>12</sup>, M. Parschau<sup>8</sup>, C. Pauly<sup>18</sup>, V. Pechenov<sup>5</sup>, O. Pechenova<sup>5</sup>, K. Piasecki<sup>16</sup>, J. Pietraszko<sup>5</sup>, T. Povar<sup>18</sup>, K. Prościński<sup>4,b</sup>, A. Prozorov<sup>14,f</sup>, W. Przygoda<sup>4</sup>, K. Pysz<sup>3</sup>, B. Ramstein<sup>13</sup>, N. Rathod<sup>17</sup>, P. Rodriguez-Ramos<sup>14,g</sup>, A. Rost<sup>5,6</sup>, A. Rustamov<sup>5,a</sup>, P. Salabura<sup>4</sup>, T. Scheib<sup>8</sup>, N. Schild<sup>6</sup>, K. Schmidt-Sommerfeld<sup>10</sup>, H. Schuldes<sup>8</sup>, E. Schwab<sup>5</sup>, F. Scozzi<sup>6,13</sup>, F. Seck<sup>6</sup>, P. Sellheim<sup>8</sup>, J. Siebenson<sup>10</sup>, L. Silva<sup>1</sup>, U. Singh<sup>4</sup>, J. Smyrski<sup>4</sup>, S. Spataro<sup>h</sup>, S. Spies<sup>8</sup>, M. Stefaniak<sup>5</sup>, H. Ströbele<sup>8</sup>, J. Stroth<sup>5,8,e</sup>, C. Sturm<sup>5</sup>, K. Sumara<sup>4</sup>, O. Svoboda<sup>14</sup>, M. Szala<sup>8</sup>, P. Tlusty<sup>14</sup>, M. Traxler<sup>5</sup>, H. Tsertos<sup>12</sup>, I. C. Udrea<sup>5,6</sup>, O. Vazquez-Doce<sup>9,10</sup>, V. Wagner<sup>14</sup>, A. A. Weber<sup>11</sup>, C. Wendisch<sup>5</sup>, M. G. Wiebusch<sup>5</sup>, J. Wirth<sup>9,10</sup>, A. Władyszewska<sup>4,b</sup>, H. P. Zbroszczyk<sup>17</sup>, E. Zherebtsova<sup>5,i</sup>, M. Zielinski<sup>4</sup>, P. Zumbbruch<sup>5</sup>, C. Curceanu<sup>i</sup>, K. Piscicchia<sup>1,j</sup>, A. Scordo<sup>i</sup>

<sup>1</sup> LIP-Laboratório de Instrumentação e Física Experimental de Partículas, 3004-516 Coimbra, Portugal

<sup>2</sup> AGH University of Krakow, Faculty of Physics and Applied Computer Science, 30-059 Kraków, Poland

<sup>3</sup> Institute of Nuclear Physics, Polish Academy of Sciences, 31342 Kraków, Poland

<sup>4</sup> Smoluchowski Institute of Physics, Jagiellonian University of Cracow, 30-059 Kraków, Poland

<sup>5</sup> GSI Helmholtzzentrum für Schwerionenforschung GmbH, 64291 Darmstadt, Germany

<sup>6</sup> Institut für Kernphysik, Technische Universität Darmstadt, 64289 Darmstadt, Germany

<sup>7</sup> Institut für Strahlenphysik, Helmholtz-Zentrum Dresden-Rossendorf, 01314 Dresden, Germany

<sup>8</sup> Institut für Kernphysik, Goethe-Universität, 60438 Frankfurt, Germany

<sup>9</sup> Excellence Cluster 'Origin and Structure of the Universe', 85748 Garching, Germany

<sup>10</sup> Physik Department E62, Technische Universität München, 85748 Garching, Germany

<sup>11</sup> II.Physikalisches Institut, Justus Liebig Universität Giessen, 35392 Giessen, Germany

<sup>12</sup> Department of Mechanical Engineering, Frederick University, 1036 Nicosia, Cyprus

<sup>13</sup> Laboratoire de Physique des 2 infinis Irène Joliot-Curie, Université Paris-Saclay. CNRS-IN2P3, 91405 Orsay, France

<sup>14</sup> Nuclear Physics Institute, The Czech Academy of Sciences, 25068 Rez, Czech Republic

<sup>15</sup> LabCAF. F. Física, Univ. de Santiago de Compostela, 15706 Santiago de Compostela, Spain

<sup>16</sup> Uniwersytet Warszawski - Instytut Fizyki Doświadczalnej, 02-093 Warszawa, Poland

<sup>17</sup> Warsaw University of Technology; Faculty of Physics, 00-662 Warsaw, Poland

<sup>18</sup> Bergische Universität Wuppertal, 42119 Wuppertal, Germany

Received: 23 January 2023 / Accepted: 19 May 2024 / Published online: 24 July 2024

© The Author(s) 2024

Communicated by Silvia Masciocchi

<sup>a</sup> Also at Instituto Politécnico de Coimbra, Instituto Superior de Engenharia de Coimbra, 3030-199 Coimbra, Portugal

<sup>b</sup> Also at Doctoral School of Exact and Natural Sciences, Jagiellonian University, Cracow, Poland

<sup>c</sup> Also at Helmholtz Research Academy Hesse for FAIR (HFHF), Campus Darmstadt, 64390 Darmstadt, Germany

<sup>d</sup> Also at Technische Universität Dresden, 01062 Dresden, Germany

<sup>e</sup> Also at Helmholtz Research Academy Hesse for FAIR (HFHF), Campus Frankfurt, 60438 Frankfurt am Main, Germany

**Abstract** Hadron production ( $\pi^\pm$ , proton,  $\Lambda$ ,  $K_S^0$ ,  $K^\pm$ ) in  $\pi^- + C$  and  $\pi^- + W$  collisions is investigated at an incident pion beam momentum of 1.7 GeV/ $c$ . This comprehensive set of data measured with HADES at SIS18/GSI significantly extends the existing world data on hadron production in pion induced reactions and provides a new reference for models that are commonly used for the interpretation of heavy-ion collisions. The measured inclusive differential production cross-sections are compared with state-of-the-art transport model (GiBUU, SMASH) calculations. The (semi-) exclusive channel  $\pi^- + A \rightarrow \Lambda + K_S^0 + X$ , in which the kinematics of the strange hadrons are correlated, is also investigated and compared to a model calculation. Agreement and remaining tensions between data and the current version of the considered transport models are discussed.

## 1 Introduction

The finite expectation values of various quark and gluon operators characterising the QCD vacuum are modified already at nuclear saturation density. As a consequence, various in-medium modifications of hadron properties are predicted [1–6]. Of particular interest for our understanding of neutron stars, such as their masses, radii, stability properties, and tidal deformability, are hadrons containing strange quarks in particular in the context of the hyperon puzzle [7–10]. The presence of hyperons in neutron stars would soften the equation of state which is difficult to reconcile with the observation of large neutron star masses  $\geq 2M_\odot$ .

Experimentally, in-medium properties of hadrons at nuclear saturation density can be studied by colliding photon-, proton-, or pion-beams with nuclear targets, for reviews see [11, 12]. The experimental challenge is to select those secondary hadrons which have stayed inside the nucleus long enough to experience a modification of their properties. Ideally, the hadron of interest is formed by the incoming beam particle on the surface of the nucleus with a subsequent long flight path through the nucleus. Hence the energy and momentum of the projectile must be appropriately chosen. Pion-induced reactions are advantageous compared to proton-induced reactions, because the inelastic  $\pi + A$  cross

section at low energies is much larger than the  $p + A$  and the momentum to energy ratio is favorable for the formation of "slow" hadrons which propagate through the nuclear medium with low probability for secondary interactions. The study of hadrons in nuclear matter provides an intermediate step between hadron formation in vacuum [13–15] and in a hot and dense system. Such an intermediate step proved to be useful for the interpretation of in-medium hadron properties deduced from heavy-ion collisions [16–23]. Data on pion induced reactions on nuclear targets at low energies are still extremely rare and mainly focus on studies of kaons [24], which are supplemented by data on proton induced reactions [25]. This work presents the inclusive spectra of  $\pi^\pm$ , proton,  $\Lambda$ ,  $K_S^0$  and  $K^\pm$  measured in  $\pi^- + C$  and  $\pi^- + W$  reactions at a pion-beam momentum of 1.7 GeV/ $c$ . This comprehensive hadron set significantly extends the existing world data on hadron production in pion induced reactions at energies of a few GeV and provides a unique testing ground for different transport models. As a light (C) and a heavy (W) nuclear target was used, our data allow us to differentiate between small and large scale medium effects.

In addition to the study of the inclusive particle production the semi-exclusive  $\pi + A \rightarrow \Lambda + K_S^0 + X$  channel was measured, in which the correlation between the kinematics of the two strange hadrons can be exploited.

The single and two-strange-particle (double-)differential spectra are compared with two state-of-the-art transport models (GiBUU [26] and SMASH [27]). It is shown that for most of the observables a satisfactory description is still lacking.

This paper is organized as follows. Section 2 gives a description of the experimental setup. Section 3 presents the analysis strategy and the results which are compared with the inclusive  $\pi^\pm$ , proton,  $\Lambda$ ,  $K_S^0$  and  $K^\pm$  spectra generated with models. Section 4 presents the details and results of the semi-exclusive analysis of the  $\pi^- + A \rightarrow \Lambda + K_S^0 + X$  channel. A summary and a conclusion is given in Sect. 5.

## 2 Experiment

The experimental data were measured with the versatile High Acceptance Di-Electron Spectrometer (HADES) at the SIS18 synchrotron at GSI Helmholtzzentrum in Darmstadt, Germany [28]. At this facility, beams can be prepared with kinetic energies between 1 and 2 AGeV for nuclei, up to 4.5 GeV for protons and 0.5–2 GeV for secondary pions. HADES consists of six identical sectors surrounding the target area covering polar angles from 18° to 85°. The azimuthal coverage varies from 65% to 90%. Each of the six sectors consists of a Ring Imaging Cherenkov (RICH) detector, followed by Multi-Wire-Drift Chambers (MDCs), two in front of and two behind a toroidal superconducting magnet, which enable the measurement of the momentum  $p$  and the specific energy loss,

<sup>f</sup> Also at Charles University, Faculty of Mathematics and Physics, 12116 Prague, Czech Republic

<sup>g</sup> Also at Czech Technical University in Prague, 16000 Prague, Czech Republic

<sup>h</sup> Also at Dipartimento di Fisica and INFN, Università di Torino, 10125 Torino, Italy

<sup>i</sup> Also at University of Wrocław, 50-204 Wrocław, Poland

<sup>j</sup> INFN, Laboratori Nazionali di Frascati, 00044 Frascati, Italy

<sup>†</sup>Deceased.

<sup>a</sup>e-mail: a.rustamov@gsi.de (corresponding author)

$dE/dx$ , of charged particles. The Multiplicity and Electron Trigger Array (META) is composed of two different time-of-flight detectors (TOF and RPC) and covers the polar angle ranges of  $44^\circ < \Theta_{TOF} < 88^\circ$  and  $12^\circ < \Theta_{RPC} < 45^\circ$ . The META is also used to provide the First Level Trigger (LVL1) signal. The measurements were conducted in 2014 with a secondary pion beam of momentum  $p_{\pi^-} = 1.7 \text{ GeV}/c$ , impinging on two nuclear targets (carbon (C) and tungsten (W)). The pions were produced in interactions of nitrogen ions with a 10 cm thick beryllium (Be) target. After extraction from the SIS18 synchrotron, the fully stripped ions had an intensity of  $\approx 10^{10}$  during the spills of 2 s duration. Behind the secondary production target, a chicane guides the  $\pi$  beam to the HADES target. Since the momentum spread of the secondary pions accepted by the chicane is about 8%, the latter is equipped with a tracking system that allows for the measurement of the momentum of each secondary  $\pi^-$ . This dedicated CERBEROS [29] setup consists of position sensitive silicon strip sensors with a high rate stability and has a momentum resolution of  $\Delta p/p < 0.5\%$ . The secondary beam had an average beam intensity of  $I_{\pi^-} \approx 3 \times 10^5 \pi^-/\text{spill}$  with an extension at the target focal point of  $\delta x \approx 1 \text{ cm}$  (rms) in agreement with simulations. The pion beam line is equipped with a mono-crystalline diamond T0 detector with a timing resolution of  $\sigma_\tau < 250 \text{ ps}$ . Both carbon and tungsten targets consisted of 3 discs with a diameter of 12 mm and thickness of 7.2 mm and 2.4 mm, respectively. During the  $\pi^-$  campaign the interaction trigger LVL1 is defined by requiring the registration of at least two hits in the META and one hit in the T0 detector. In total,  $1.3 \times 10^8 \pi^- + \text{C}$  and  $1.7 \times 10^8 \pi^- + \text{W}$  interactions were recorded. Charged particle trajectories were reconstructed using the hits measured in the MDCs. The resulting tracks were subjected to several selections based on quality parameters delivered by a Runge–Kutta track fitting algorithm [28]. Their momentum resolution ( $\Delta p/p$ ) is approximately 3% [28].

### 3 Inclusive data analysis

In this section we present the analysis of the inclusive (double-)differential production cross section of  $\pi^\pm$ , proton,  $\Lambda$  and  $K_S^0$ . To provide a more complete picture of strange hadron production, the (double-)differential production cross section of  $K^+$  and  $K^-$  taken from [30] are presented as well. The obtained differential cross sections are compared with two state-of-the-art transport models, the Giessen Boltzmann–Uehling–Uhlenbeck (GiBUU) [26] model and the Simulating Many Accelerated Strongly-Interacting Hadrons (SMASH) [27] model.

### 3.1 Event selection and particle identification

Only events with a reconstructed primary vertex (PV) in the target region are considered in the analysis. The identification of charged particles is based on momentum and time-of-flight measurements by exploiting the relation  $p/\sqrt{p^2 + m_0^2} = \beta$ , with  $m_0$  being the nominal mass of  $\pi^+$ ,  $\pi^-$  or proton [31, 32]. The energy loss measured in the MDCs is used only in the semi-exclusive analysis discussed in Sect. 4.

#### 3.1.1 Charged pions and protons

The charged pions are identified within a window of a  $\pm 2\sigma$  around the pion peak in the  $\beta$  distributions in different of  $p$  intervals, separately for TOF and RPC. To reduce the systematic uncertainty of the momentum reconstruction and of the PID, the momentum of the charged pions is restricted to  $p_{\pi^\pm} < 1000 \text{ MeV}/c$ . Using full-scale detector-response Geant3 simulations as a reference, an average  $\pi^\pm$  purity of 95% and 88% is found for the  $\pi^- + \text{C}$  and  $\pi^- + \text{W}$  reactions, respectively. In order to ensure that the efficiency correction takes into account the effects of residual impurities from misidentification, the  $p_T - y$  intervals were excluded from the analysis when the purity in experiment and simulation deviated by more than  $\pm 5\%$ . Note, that the mass resolution is found to be in agreement between simulation and experiment within 8%. The numerical values of the correction factors for each  $p_T - y$  interval can be looked up in [32].

The  $\pi^\pm$  yield is obtained by integrating the mass distributions for the different  $p_T - y$  intervals. The total number of reconstructed  $\pi^+$  and  $\pi^-$  within the HADES acceptance in  $\pi^- + \text{C}$  is  $N_C^{\pi^+} = (11.4 \pm 0.003) \times 10^6$  and  $N_C^{\pi^-} = (27.6 \pm 0.005) \times 10^6$ , and in  $\pi^- + \text{W}$  collisions  $N_W^{\pi^+} = (9.0 \pm 0.003) \times 10^6$  and  $N_W^{\pi^-} = (23.3 \pm 0.005) \times 10^6$ , respectively.

Similar to the charged pions, the protons were identified by a  $\pm 2\sigma$  window around the nominal  $\beta$  vs.  $p$  correlation. By integrating the measured mass distributions the proton yield is extracted for each  $p_T - y$  interval. On the basis of full-scale Geant simulations the proton purity is found to be above 99% for both colliding systems. The total number of reconstructed protons within the HADES acceptance is equal to  $N_C^p = (30.5 \pm 0.006) \times 10^6$  and  $N_W^p = (56.1 \pm 0.007) \times 10^6$  in  $\pi^- + \text{C}$  and  $\pi^- + \text{W}$  collisions, respectively.

#### 3.1.2 $\Lambda$ and $K_S^0$

The inclusive production of the neutral strange hadrons,  $\Lambda$  and  $K_S^0$ , is investigated via their charged decay channels  $\Lambda \rightarrow \pi^- p$  ( $BR \approx 63.9\%$  [33]) and  $K_S^0 \rightarrow \pi^+ \pi^-$  ( $BR \approx 69.2\%$  [33]). It has to be noted that the reconstructed  $\Lambda$

yield contains also a contribution from the (slightly heavier)  $\Sigma^0$  hyperon, which is decaying electromagnetically (almost) exclusively into a  $\Lambda$  together with a photon. Hence, “ $\Lambda$  yield” has to be understood as that of  $\Lambda + \Sigma^0$  throughout the paper.

Each daughter particle is identified applying a  $\beta$  vs. momentum selection of  $|p/\sqrt{p^2 + m_0^2} - \beta| < 0.2$  and the invariant mass of the  $\Lambda$  ( $K_S^0$ ) candidates is calculated using the nominal masses for the selected daughter particles. To maximize the signal-to-background ratio ( $S/B$ ) of both neutral strange hadrons and to minimize the contribution by off-target reactions, additional topological selections were applied. The position of the PV is calculated event-by-event by taking the point of closest approach (PCA) of the reconstructed  $\Lambda$  or  $K_S^0$  trajectories and the beam axis. The secondary decay vertex (SV) corresponds to the PCA of the daughter tracks. Three additional topological selections are employed to enhance the  $\Lambda$  ( $K_S^0$ ) signal and reduce the combinatorial background: (i) the  $z$  coordinate of the SV has to be downstream with respect to the PV ( $z_{PV} < z_{SV}$ ), (ii) the distance  $d$  of closest approach (DCA) between the decay particle trajectories and the PV has to fulfill the following conditions:  $d_p > 5$  mm and  $d_{\pi^-} > 18$  mm for the  $\Lambda$  decays and  $d_{\pi^\pm} > 4.5$  mm for the  $K_S^0$  decays. (iii) the DCA between the trajectories of the two decay particles has to be smaller than 10 mm for the  $\Lambda$  decays and 6 mm for the  $K_S^0$  decays.

Figure 1 shows an example of the resulting invariant mass distributions for  $\Lambda$  (panel (a)) and  $K_S^0$  (panel (b)) for a selected phase-space interval. For each  $p_T - y$  interval the  $\Lambda$  signal in the invariant mass distributions is modelled by the sum of two Gaussian functions, and the background by a third degree polynomial. The signal width is in this case calculated by evaluating the weighted average of the widths of the two Gaussian. The  $K_S^0$  invariant mass is fitted with a single Gaussian and a third-order polynomial. The particle yields were obtained by integrating the signal functions within a  $\pm 3\sigma$  region. The mass and resolution are found to be  $\mu_\Lambda = 1114.7$  MeV/ $c$ ,  $\sigma_\Lambda = 2.3$  MeV/ $c$ , respectively  $\mu_{K_S^0} = 495.7$  MeV/ $c$  and  $\sigma_{K_S^0} = 6.95$  MeV/ $c$  and the agreement between experiment and simulation is better than 7% over the whole phase-space. Typical signal-to-background ratios are 8.6 for  $\Lambda$  and 2.1 for  $K_S^0$  candidates. The total numbers of reconstructed  $\Lambda$  and  $K_S^0$  within the HADES acceptance in  $\pi^- + C$  collisions correspond to  $N_\Lambda(C) = (66.2 \pm 0.3) \times 10^3$  and  $N_{K_S^0}(C) = (58.6 \pm 0.4) \times 10^3$ , and in  $\pi^- + W$  collisions to  $N_\Lambda(W) = (79.9 \pm 0.3) \times 10^3$  and  $N_{K_S^0}(W) = (64.1 \pm 0.3) \times 10^3$ .

### 3.2 Double-differential cross sections

The obtained double-differential inclusive yields of the five species  $\pi^+$ ,  $\pi^-$ ,  $p$ ,  $\Lambda$ ,  $K_S^0$  were corrected for the losses due to inefficiencies of the reconstruction and to limited acceptance.

The average combined acceptance and efficiency of  $\pi^+(\pi^-)$  is 50% (40%) for both collision systems, while the average combined proton acceptance and efficiency is around 56% (50%) for  $\pi^- + C(W)$  collisions. For  $\Lambda$  and  $K_S^0$  the average efficiency is 3.8% and 6.3%, respectively. The numerical values of the correction factors for each  $p_T - y$  interval can be looked up in [31].

The validity and systematic uncertainty of the efficiency correction based on the simulated detector response of HADES is checked by means of an additional data sample recorded for pions with a momentum of  $p_{\pi^-} = 0.69$  GeV/ $c$  impinging on a solid  $12 \times 44$  mm<sup>2</sup> polyethylene (C<sub>2</sub>H<sub>4</sub>) target which allowed to carry out the analysis of the exclusive elastic interaction channel,  $\pi^- + p \rightarrow \pi^- + p$  [34]. By exploiting the kinematic constraints of the elastic reaction, it is possible to extract a data-driven detector efficiency map. It is found that both, experimental and simulated efficiencies are consistent within 3%. The observed difference is used as estimate of the systematic uncertainty. Residual effects of PID, not accounted for by the efficiency correction, have been checked for by varying the selection in the velocity vs. momentum plane between  $\pm 1.5\sigma$ ,  $2\sigma$  and  $2.5\sigma$ . The observed differences are smaller than 1% and are neglected.

To obtain the absolute cross sections, the corrected yields were normalized to the total number of beam particles and the target density. The normalization uncertainty due to the uncertainty of the beam intensity on the target is estimated to be about 14% [31].

In the case of the  $\Lambda$  and the  $K_S^0$  the additional systematic uncertainties caused by the decay topology selection are estimated by varying the selection criteria within 20%. The resulting uncertainties are estimated separately for each  $p_T - y$  interval. Table 1 presents the average, the lowest and highest values for each hadron and collision system. The resulting systematic uncertainty for the  $\Lambda$  and the  $K_S^0$  represents the quadratic sum of the values estimated via the decay

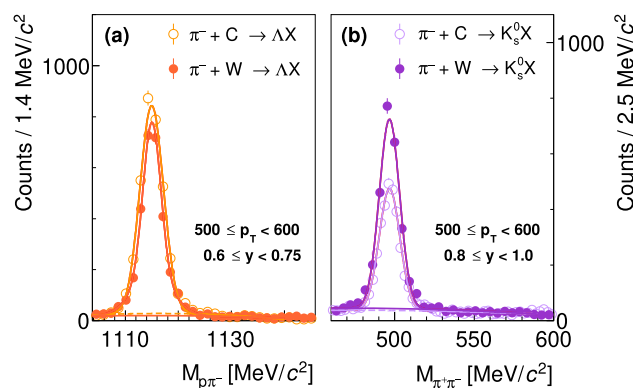


**Fig. 1** Invariant mass distributions of  $p\pi^-$  (a) and  $\pi^+\pi^-$  pairs (b) in  $\pi^- + C$  (open points) and  $\pi^- + W$  (solid points) collisions for the representative phase-space interval given in the legend. Lines are fits to the data, see text for details

**Table 1** Mean values of uncertainties in percent for the  $\pi^- + C$  and  $\pi^- + W$  systems. In parenthesis, the minimum and maximum values are provided

	C	W
$\Lambda$	2.8 (1.8–39.8)	3.8 (0.5–79.6)
$K_S^0$	1.4 (0.2–45.2)	1.6 (0.4–44.8)

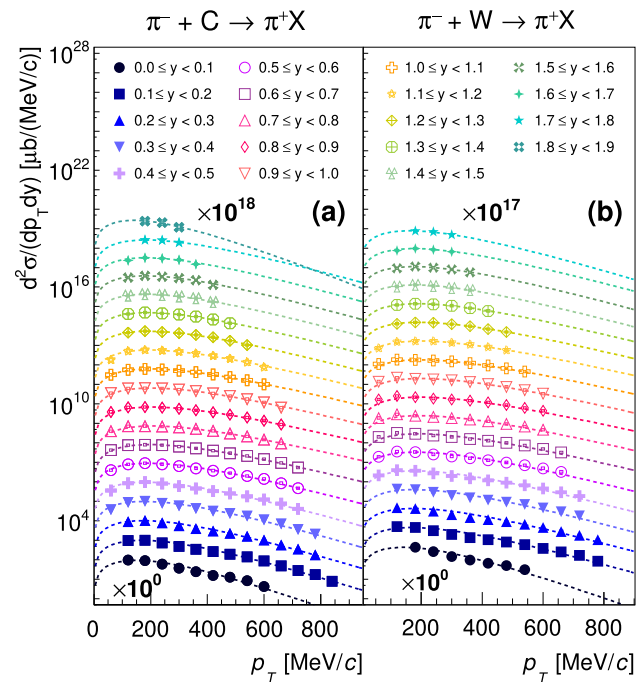


**Fig. 2** Differential  $\pi^+$  cross sections in subsequent rapidity intervals in the laboratory frame (see legend). The left panel corresponds to  $\pi^- + C$  reactions, while the right panel to  $\pi^- + W$  reactions. For a better representation, the spectra are scaled by consecutive factors of 10 for each rapidity interval ( $10^0$  for  $0 \leq y < 0.1$ ). The normalization uncertainty (open boxes), the systematic uncertainties (shaded band) and the statistical errors (vertical lines) are smaller than the symbol size for most of the data points. The dashed curves correspond to Boltzmann fits (see text for details)

topology and the estimated value for the efficiency correction of 3%.

Throughout the paper the normalization uncertainty is plotted in the form of open boxes, the systematic uncertainties as a shaded band and the statistical errors as vertical lines. Note that in various plots, the uncertainties are smaller than the symbol size.

The resulting double-differential cross sections for  $\pi^+$  emission in  $\pi^- + C$  (Fig. 2a) and  $\pi^- + W$  (Fig. 2b) collisions are shown for 19 (18) rapidity intervals subdividing the range  $0 < y < 1.9$  (1.8). Analogously to the  $\pi^+$ , the  $\pi^-$  results are presented in Fig. 3 for 18 rapidity intervals subdividing the range  $0.1 < y < 1.9$ .

For the protons the resulting double-differential cross sections in  $\pi^- + C$  (Fig. 4a) collisions are shown for 10 rapidity

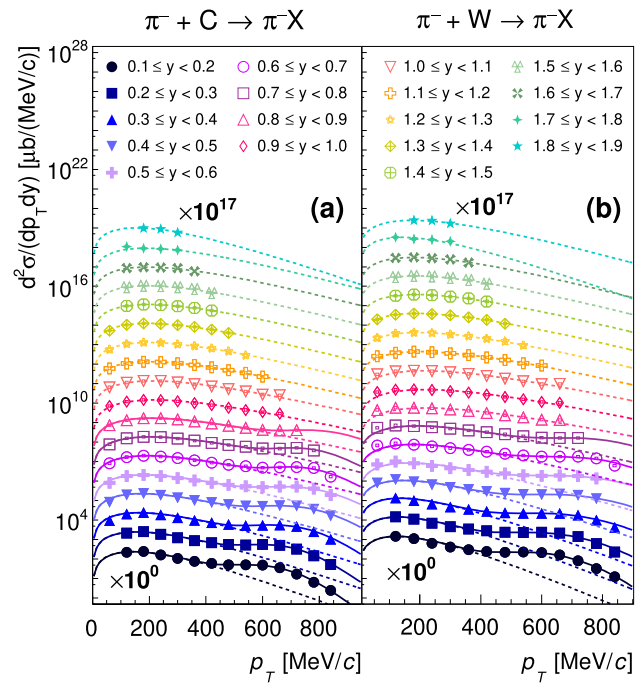


**Fig. 3**  $\pi^-$  double-differential cross sections in subsequent rapidity intervals (see legend). The left panel corresponds to  $\pi^- + C$  reactions, while the right panel to  $\pi^- + W$  reactions. For a better representation, each spectrum is scaled by consecutive factors of 10 for each rapidity range ( $10^0$  for  $0.1 \leq y < 0.2$ ). The normalization uncertainty (open boxes), the systematic uncertainties (shaded band) and the statistical errors (vertical lines) are smaller than the symbol size for most of the data points. In the lower rapidity region ( $y \lesssim 0.8$ ), the inelastic (low  $p_T$ ) and (quasi-)elastically scattered (high  $p_T$ )  $\pi^-$  contribute to the transverse momentum spectra. The dashed curves correspond to Boltzmann fits, while the solid curves represent the combined Boltzmann and Gaussian fits (see text for details)

intervals subdividing the range  $0 < y < 1.0$ . For  $\pi^- + W$  (Fig. 4b) collisions 9 rapidity intervals subdividing the range  $0 < y < 0.9$  are displayed.

The resulting double-differential cross sections for  $\Lambda$  in  $\pi^- + C$  (Fig. 5a) and  $\pi^- + W$  (Fig. 5b) collisions are shown in Fig. 5 for 7 rapidity intervals subdividing the range  $0 < y < 1.05$ . Figure 6 depicts the analog for the  $K_S^0$  with 8 rapidity intervals in the range  $0 < y < 1.6$ . The uncertainties in Figs. 2, 3, 4, 5, 6 represent the normalization uncertainty (open boxes), the systematic uncertainties (shaded band) and the statistical errors (vertical lines) and are smaller than the symbol size for most of the data points.

### 3.3 $p_T$ -integrated cross sections

The respective  $p_T$  integrated cross section per rapidity interval is calculated in the following way; The integration of the measured cross sections is complemented with extrapolations in the low- and high- $p_T$  regions not covered by HADES by employing a Boltzmann fit to the mea-

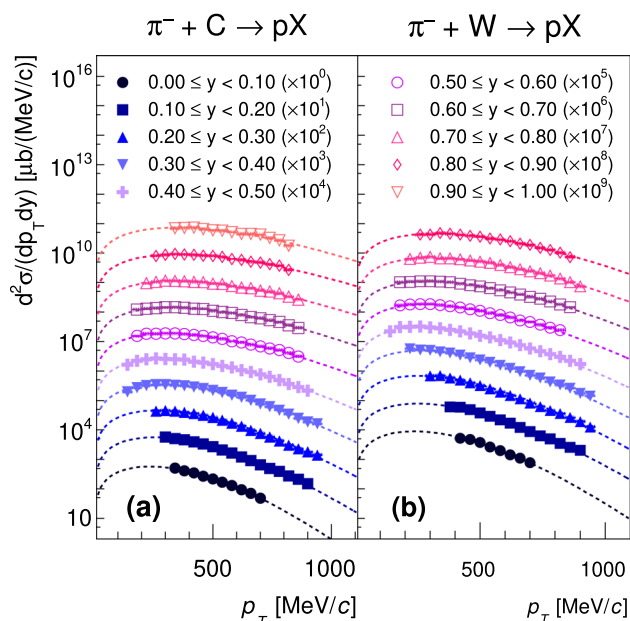


**Fig. 4** Double-differential proton cross sections in different rapidity intervals (see legend). The representation is analogous to Fig. 2

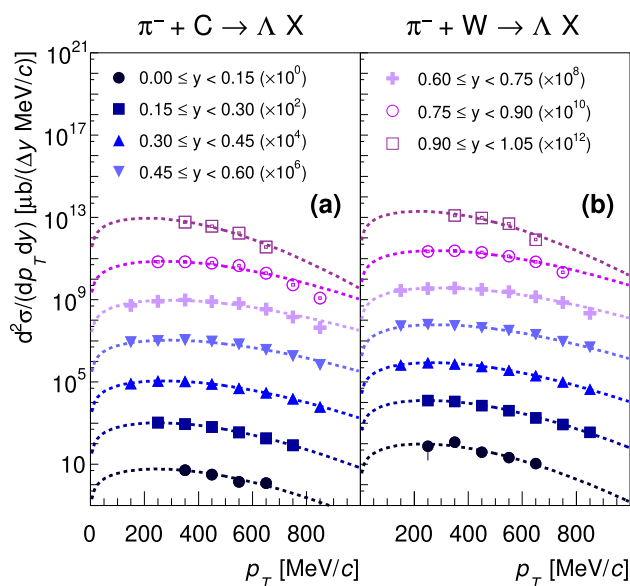


**Fig. 5** Double-differential  $\Lambda$  cross sections in different rapidity intervals (see legend). The representation is analogous to Fig. 2

sured distributions. The function reads  $d^2N/(dp_T dy) = C(y) \cdot p_T \cdot \sqrt{p_T^2 + m_0^2} \exp(-\sqrt{p_T^2 + m_0^2}/T_B(y))$ , where  $C(y)$  denotes a scaling factor,  $m_0$  is again the respective nominal mass and  $T_B(y)$  stands for the inverse slope parameter. The relatively modest modifications of the spectra by the Coulomb field of the nucleus [35] are small compared to the applied systematic uncertainties. For the negatively charged pions the extrapolation is more complex, since also (quasi)-elastically scattered  $\pi^-$  contribute. Hence, in addition to the

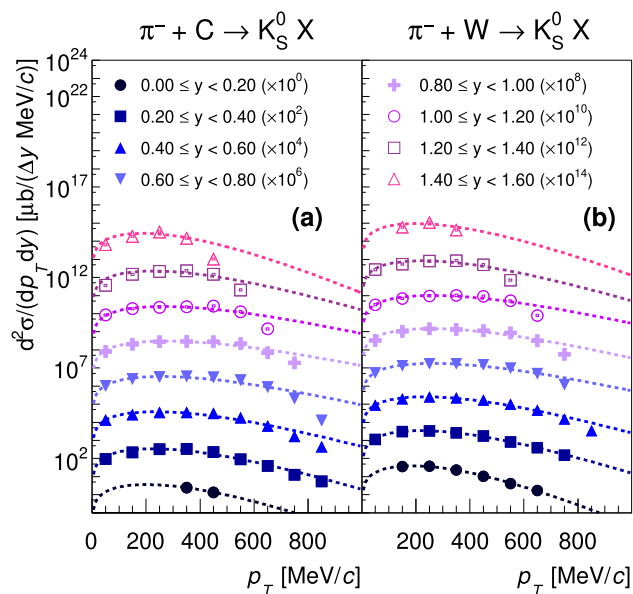


**Fig. 6** Double-differential  $K_S^0$  cross sections in different rapidity intervals (see legend). The representation is analogous to Fig. 2

**Table 2** Target, particle species and cross section integrated inside the rapidity range covered by HADES. Error values shown are statistical (first), systematic (second) and normalization (third)

Target	Particle	$y$ range	$\Delta\sigma$ [ $\mu\text{b}$ ]
C	$\Lambda$	0.0–1.05	$(4.3 \pm 0.02 \pm 0.13 \pm 0.65) \times 10^3$
C	$K_S^0$	0.0–1.6	$(2.0 \pm 0.01 \pm 0.08 \pm 0.3) \times 10^3$
C	$\pi^+$	0.0–1.9	$(44 \pm 0.01 \pm 1.3 \pm 6.6) \times 10^3$
C	$p$	0.0–1.0	$(133 \pm 0.02 \pm 21 \pm 20) \times 10^3$
W	$\Lambda$	0.0–1.05	$(30 \pm 0.13_{-1.1}^{+0.68} \pm 4.5) \times 10^3$
W	$K_S^0$	0.0–1.6	$(13 \pm 0.06_{-0.28}^{+0.3} \pm 2) \times 10^3$
W	$\pi^+$	0.0–1.8	$(153 \pm 0.05_{-5.6}^{+4.6} \pm 23) \times 10^3$
W	$p$	0.0–0.9	$(156 \pm 0.02 \pm 56 \pm 23) \times 10^4$

Boltzmann fit for the inelastic reactions (low  $p_T$ ), a Gaussian fit is used for the elastic events (high  $p_T$ ). However, for  $y \lesssim 0.8$  the part of the  $p_T$  distribution corresponding to the (quasi)-elastically scattered  $\pi^-$  is outside of the HADES acceptance, and hence only the inelastic part can be extrapolated. In order to extract the inelastic yield over the entire covered rapidity range, all measured data points were summed up in the inelastic range up to  $p_T = 390$  MeV/c for  $y \lesssim 0.8$ . On the other hand, the  $p_T$  coverage for the protons is larger, and the enhancement due to the (quasi)-elastic reaction channel is less pronounced. Therefore, no Gaussian fit is needed for the extrapolation. As demonstrated in Figs. 2, 3, 4, 5, 6 the fits based on an exponential function describe the experimental data with reasonable agreement, which is in line with simulation studies with our event generator Pluto [36] in which the Fermi motion inside the nucleus is taken into account [32].

**Table 3** As in Table 2 but for  $\pi^-$

Target	Particle	y range	$\Delta\sigma$ [ $\mu\text{b}$ ]
C	$\pi^-$ (tot)	0.1–0.9	$(57 \pm 0.01_{-1.9}^{+1.7} \pm 8.6) \times 10^3$
C	$\pi^-$ (inelastic)	0.1–1.9	$(94 \pm 0.02_{-3}^{+2.8} \pm 14.1) \times 10^3$
W	$\pi^-$ (tot)	0.1–0.8	$(214 \pm 0.06 \pm 6.5 \pm 32) \times 10^3$
W	$\pi^-$ (inelastic)	0.1–1.9	$(348 \pm 0.08 \pm 11 \pm 52) \times 10^3$

The extrapolation of the  $\pi^+$ ,  $\pi^-$ ,  $p$ ,  $\Lambda$  and  $K_S^0$  yields over the entire  $p_T$  range allowed to extract the rapidity distributions shown in Figs. 14, 15, 16. The integrated differential production cross sections  $\Delta\sigma$ , in the rapidity ranges covered by HADES ( $0 \leq y < 1.05$  for  $\Lambda$ ,  $0 \leq y < 1.6$  for  $K_S^0$ ,  $0 \leq y < 1.9$  (1.8) for  $\pi^+$  and  $0 \leq y < 0.9$  for  $p$ ), in  $\pi^- + C$  ( $W$ ) reactions are listed in Table 2. The error values shown correspond to the statistical (first), systematic (second) and normalization (third) contribution. The systematic uncertainties of  $p_T$ -integrated cross-sections contain also the uncertainties of the extrapolation in the  $p_T$ , estimated by varying the extrapolation function and the minimization method. This uncertainty is again added as quadratic sum to the total systematic uncertainty.

Moreover, the integrated differential inelastic (total) production cross sections  $\Delta\sigma$  for  $\pi^-$  ( $0.1 \leq y < 1.9$  (0.9/0.8)) in both collision systems inside the covered rapidity range are given in Table 3.

### 3.4 Comparison to transport model calculations<sup>4</sup>

Testing, validating and tuning of models is huge effort [37–39]. Therefore, we restrict ourselves to a comparison of observables, which we hope to serve as bench marks for more involved studies of e.g. including the kaon-nucleon in-medium interaction [40].

Figures 7, 8, 9, 10, 11, 12, 13, 14, 15, 16 show the comparison of the measured differential cross sections as a function of transverse momentum  $p_T$  as well as rapidity  $y$  with the hadronic transport models GiBUU (v2017) [26] and SMASH (v1.6) [27]. Both models are run without the inclusion of in-medium potentials for strange hadrons. The production mechanisms employed in these transport models differ. In GiBUU, hadron production channels are directly parameterized based on the measured cross sections. Depending on the production channels, SMASH uses an explicit treatment with intermediate baryon resonances or parametrizations similar to the GiBUU model. The elementary strange hadron production channels are listed in Table 4. The corresponding cross section ( $\sigma_{fit}$ ) is given for each channel at the incident pion momentum of 1.7 GeV/c. The cross section is extracted by applying the parametrization given in [41,42], to interpolate the experimental data to the given beam momentum.

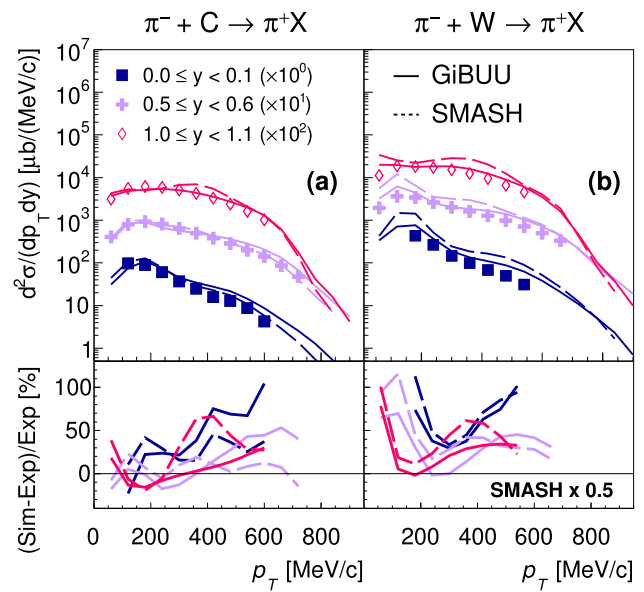


**Fig. 7** Upper panel: (Double-)differential cross sections of  $\pi^+$  as a function of the transverse momentum  $p_T$  in  $\pi^- + C$  (a) and  $\pi^- + W$  (b) reactions compared with GiBUU (solid curves) and SMASH (long-dashed curves) for different rapidity intervals (see legend). The normalization uncertainty (open boxes), the systematic uncertainties (shaded band) and the statistical errors (vertical lines) are smaller than the symbol size for most of the data points. Lower panel: relative deviations between experimental data and the two transport model calculations. For better visibility the deviations to the SMASH calculation are scaled with the factor 0.5

In addition, the cross sections implemented in GiBUU and SMASH are listed. In all the following figures, the results of the GiBUU calculation are represented by solid curves, while the ones of SMASH are depicted by long-dashed curves. The upper panels present the comparison of the experimental data with the model calculations in a logarithmic scale, while the lower panels show the deviation between the measured and simulated distributions expressed as the relative difference normalised to the experimental cross section ((Sim-Exp)/Exp) in a linear scale.

#### 3.4.1 Pions and protons

Considering first  $\pi^+$ , Fig. 7 shows the comparison between the measured differential cross sections as a function of transverse momentum  $p_T$  with GiBUU (solid curve) and SMASH (long-dashed curve) results for low (0.0–0.1), intermediate (0.5–0.6) and high (1.0–1.1) rapidity regions in  $\pi^- + C$  (Fig. 7a) and  $\pi^- + W$  (Fig. 7b) collisions. In general, both models describe the shapes of the  $p_T$  distribution for  $\pi^+$  similarly well, with difference smaller than 50%. The yields from the models are systematically higher than those in the experimental data by about 25%, with deviations as large as a factor of 2 (3) at low and high  $p_T$  in the heavy target case for GiBUU (SMASH) data. The  $\pi^+$  production cross section as function of rapidity is included in Fig. 14, together with

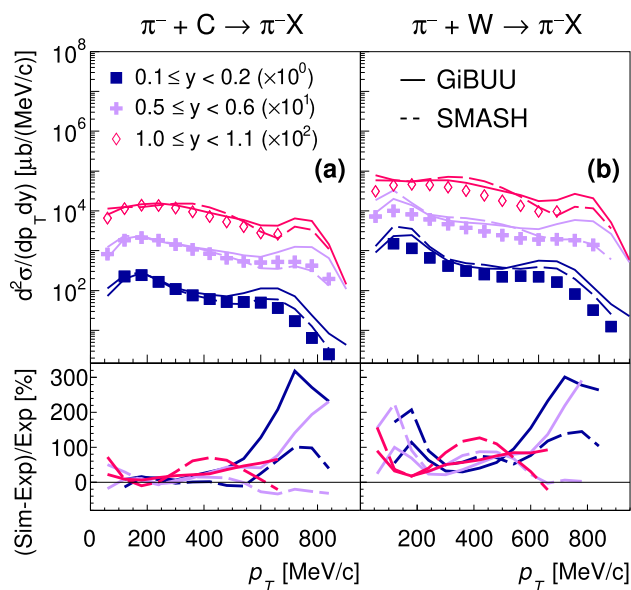


**Fig. 8** Comparison of the  $\pi^-$  differential cross sections as a function of the transverse momentum with GiBUU (solid curves) and SMASH (long-dashed curves). The representation is analogous to Fig. 7

the model predictions. The model calculations differ by up to 50% over the whole considered rapidity range for the heavy target case and only at forward rapidities for the light target case. The relative differences with respect to the experimental data stay below 100% in the former and 50% in the latter case.

The  $\pi^-$  differential cross sections as a function of  $p_T$  are compared to the GiBUU (solid curve) and SMASH (long-dashed curve) calculations for low (0.1–0.2), intermediate (0.5–0.6) and high rapidity (1.0–1.1) regions in  $\pi^- + \text{C}$  (Fig. 8a) and  $\pi^- + \text{W}$  (Fig. 8b) collisions, respectively. The general features are similar to the ones observed for  $\pi^+$  production. However, there is in addition the (quasi-)elastic scattering process which contributes to the measured  $\pi^-$  cross section. The corresponding enhancement is visible in the high- $p_T$  region and more pronounced in the model results than in the experimental data by a factor of two for SMASH and three for GiBUU.

In particular, in the high- $p_T$  region, corresponding to the (quasi-)elastic scattering events, both theoretical predictions significantly overestimate the experimental data. The comparison of the  $\pi^-$  cross section as a function of rapidity with the models is shown in Fig. 15. Both models reproduce the experimental data within 30% for the small target nucleus. In the tungsten case the cross section found by the models is by a factor of two higher than the experimental data.

For technical reasons, protons are only compared to the GiBUU calculations. Figure 9 shows the proton differential cross sections as a function of  $p_T$  compared with the predictions, for low (0.1–0.2), intermediate (0.4–0.5) and high

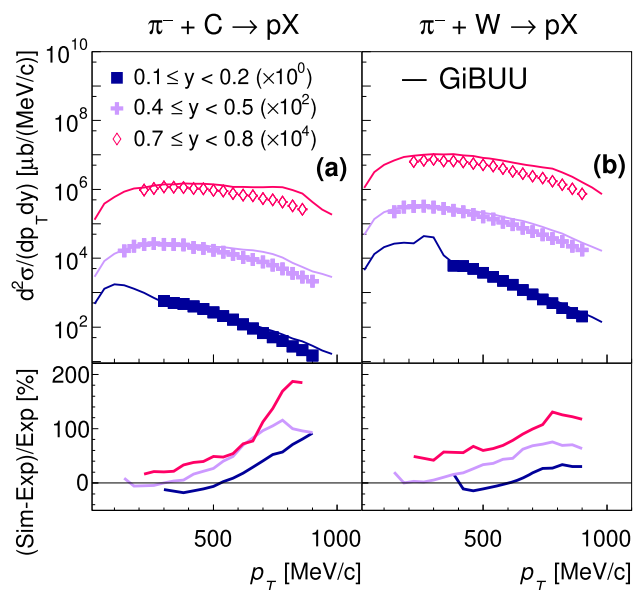


**Fig. 9** Comparison of the proton differential cross sections as a function of the transverse momentum with GiBUU (solid curves). The representation is analogous to Fig. 7

(0.7–0.8) rapidity regions in  $\pi^- + \text{C}$  (panel (a)) and  $\pi^- + \text{W}$  (panel (b)) collisions, respectively. For both colliding systems, the proton yield is overestimated by the GiBUU model, in particular at high  $p_T$  where it is higher by a factor of roughly 2.0 (1.6) in the case of C (W) target. Note that GiBUU does not form composite objects, hence a part of the proton excess is due the neglected binding of protons in light nuclei. A hint at the expected enhancement due to elastic events is visible in the model calculations in the lowest rapidity interval, but in a region which is not covered by the experimental data. The experimental proton cross section as a function of rapidities is presented in Fig. 14 together with the GiBUU calculations, which overshoots the data by a factor of 3 (2) only near target rapidity in the carbon (tungsten) case.

### 3.4.2 Strange hadrons

In Fig. 10 the experimental  $p_T$  distributions of  $\Lambda$  are compared with the models for low (0.0–0.15), medium (0.45–0.6) and high (0.9–1.05) rapidities. Similar shapes and absolute cross sections are observed for GiBUU and SMASH. However, the values predicted by the models are systematically below the measured ones for both collision systems, except for the high rapidity interval.

Figure 14 shows different rapidity distributions for the  $\Lambda$  production with C (panel (a)) and W (panel (b)) targets. While in case of C target most of the yield is inside the rapidity range covered by HADES, the  $\Lambda$  hyperons experience backward scattering in the W target. Also here, the model calculations do not agree well with the experimental distributions. Both



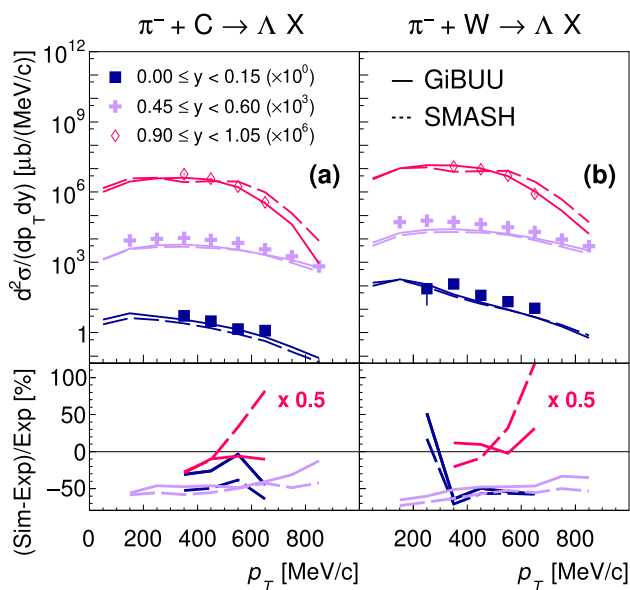


**Fig. 10** Comparison of the  $\Lambda$  differential cross sections as a function of the transverse momentum with GiBUU (solid curves) and SMASH (long-dashed curves). The representation is analogous to Fig. 7. Lower panel: deviations between transport models and data. For better visibility the deviations in the forward interval are scaled with the factor 0.5

models predict a double-hump structure for the lighter target, not seen in the experimental data. The calculated cross section in  $\pi^- + \text{C}$  ( $\pi^- + \text{W}$ ) underestimates the data by up to 50% (60%).

For the heavier target both models show similar distributions, again a double-hump structure, in contrast to the experimental data and underestimate the cross section. Summarizing, a precise theoretical description of the double-differential  $\Lambda$  production cross sections is missing.

For the  $K_S^0$ , the comparison of the differential cross section as a function of  $p_T$  is depicted in Fig. 11 for backward ( $0.20-0.40$ ), middle ( $0.60-0.80$ ) and forward ( $1.00-1.20$ ) rapidity. For the GiBUU model an overall good agreement of the shape and cross section is observed in both collision systems with minor deviations for  $p_T \geq 600 \text{ MeV}/c$ . SMASH overshoots the experimental data over the entire  $p_T$  range in both collision systems. In Fig. 16, the  $K_S^0$  rapidity distribution for  $\pi^- + \text{C}$  (panel (a)) and  $\pi^- + \text{W}$  (panel (b)) collisions is shown. The two experimental distributions have different shapes. Similar to the  $\Lambda$ , they are shifted to backward rapidity in reactions with the heavier target. The result of the GiBUU model is consistent with the experimental data also as function of rapidity over (almost) the entire range. SMASH overestimates the cross section over the entire rapidity range by a factor of 2 (4) for reactions with the Carbon (Tungsten) target.

Both models are also compared with the recently published differential  $K^+$  production cross sections obtained for

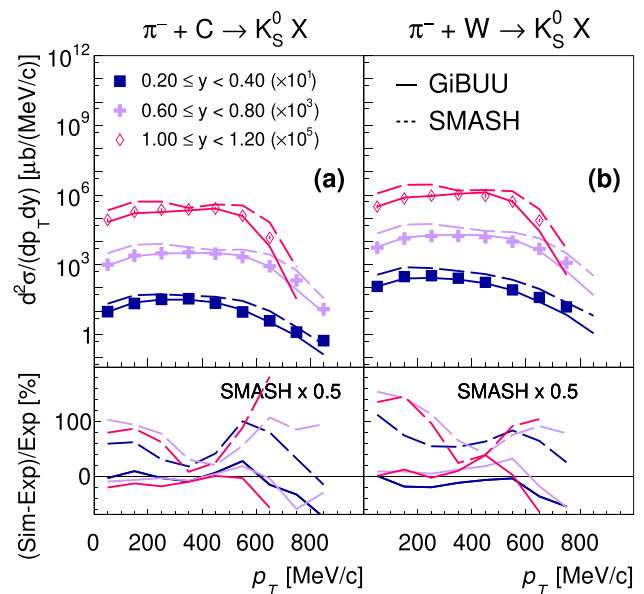


**Fig. 11** Comparison of the  $K_S^0$  differential cross sections as a function of the transverse momentum with GiBUU (solid curves) and SMASH (long-dashed curves). The representation is analogous to Fig. 7. Lower panel: deviation of the transport models calculations to the experimental data as a function of rapidity. For better visibility the deviations in the SMASH case are scaled with the factor 0.5

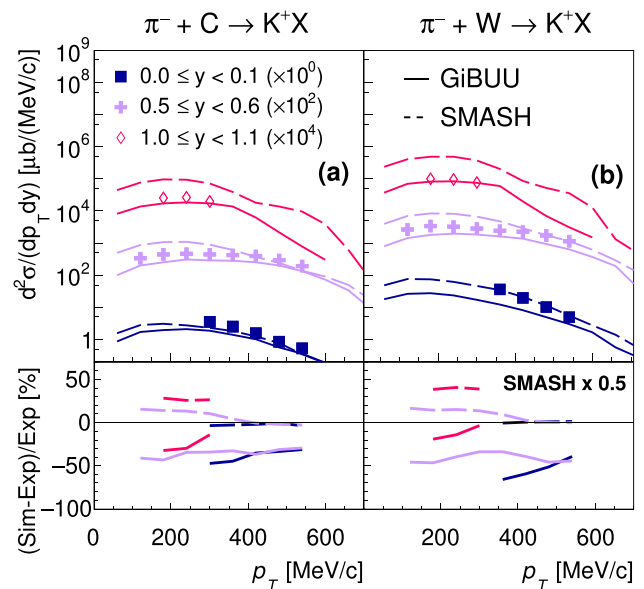


**Fig. 12** Comparison of the  $K^+$  differential cross sections [30] as a function of the transverse momentum to GiBUU (solid curves) and SMASH (long-dashed curves). The representation is analogous to Fig. 7. The deviations to SMASH in the lower right panel are scaled with the factor 0.5

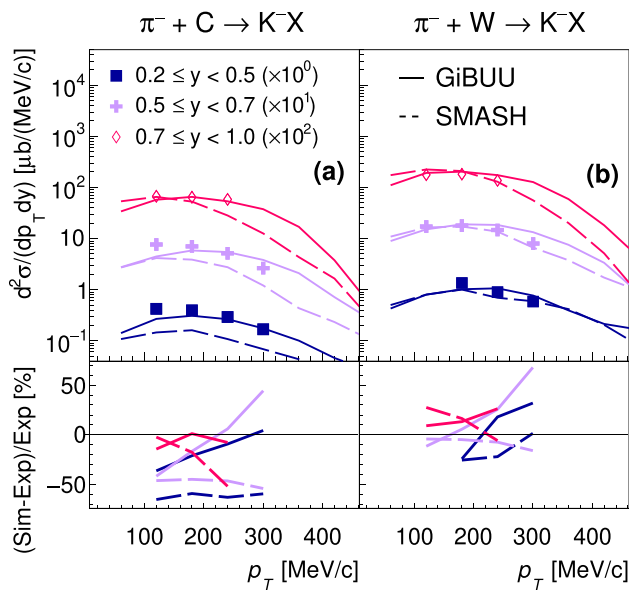


**Fig. 13** Comparison of the  $K^-$  differential cross sections [30] as a function of the transverse momentum to GiBUU (solid curves) and SMASH (long-dashed curves). The representation is analogous to Fig. 7

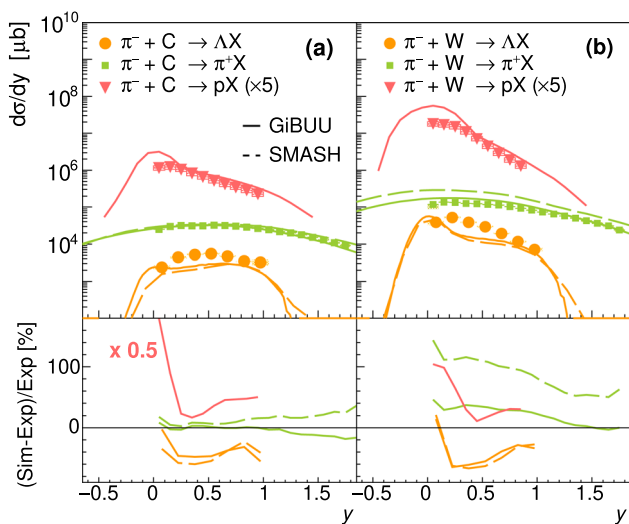


**Fig. 14** Upper panel: cross section of  $\Lambda$  (orange points),  $\pi^+$  (green squares) and  $p$  (red triangle) as a function of rapidity in  $\pi^- + C$  (a) and  $\pi^- + W$  (b) reactions compared with the transport models, GiBUU (solid curve) and SMASH (long-dashed curve). The shaded bands denote the systematic uncertainties. The open boxes indicate the normalization uncertainty. The statistical uncertainties are smaller than the symbol size. Lower panel: deviations of the three transport models from the measured cross section of  $\Lambda$  ( $\pi^\pm$ ,  $p$ ) as a function of rapidity. For better visibility the deviations for protons from GiBUU are scaled with factor 0.5

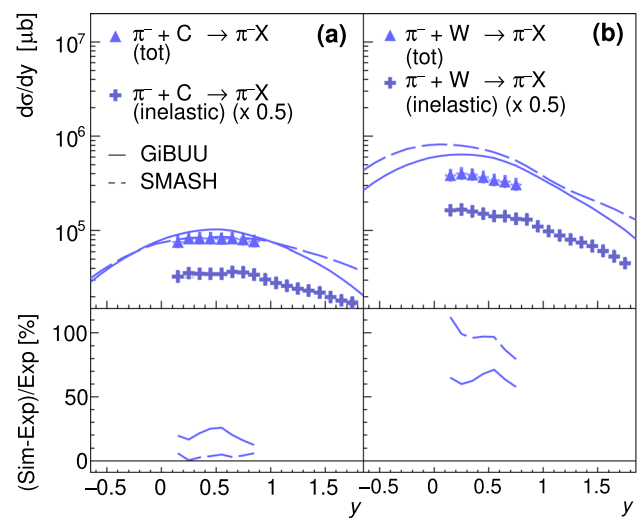


**Fig. 15** Comparison of the total (triangles) and inelastic (crosses)  $\pi^-$  differential cross sections as a function of rapidity with GiBUU (solid curves) and SMASH (long-dashed curves). The representation is analogous to Fig. 14

the same collision systems [30]. In Fig. 12 the  $K^+$  differential cross section as a function of  $p_T$  is shown for backward (0.0–0.1), middle (0.5–0.6) and forward (1.0–1.1) rapidity. GiBUU underestimates the  $K^+$  cross-section in  $\pi^- + C$  (panel (a)) and  $\pi^- + W$  (panel (b)) collisions over the entire  $p_T$  and rapidity range by up to 50%. Except for the region close to target rapidity, the SMASH results exceed the experimental cross section in both nuclear reactions by up to 80%. The  $K^+$  cross section is presented as a function of the rapidity in Fig. 16 together with the results of the model calculations. GiBUU describes the data rather well with deviations of only 20% to 60%, whereas SMASH exhibits a different shape with agreement near target rapidity and a deviation of up to a factor of 5 at the highest measured rapidity. The model calculations of  $K^+$  and  $K_S^0$  production shown in Fig. 16 are significantly different: SMASH finds very similar shapes and sizes of the two rapidity distributions resulting in an almost constant  $K^+/K_S^0$  cross section ratio (close to unity) as a function of rapidity. The GiBUU ratios, however, increase significantly from close to unity near target rapidity to 10 at high rapidity. This trend is also seen in the experimental data.

The set of kaons are completed with the comparison for charged antikaons [30]. Figure 13 presents the differential  $K^-$   $p_T$ -differential cross sections for three measured rapidity intervals, 0.2–0.5, 0.5–0.7 and 0.7–1.0. For both colliding systems, GiBUU reproduces the shape of the experimental spectra rather well. The cross section is slightly underestimated at low  $p_T$  in  $\pi^- + C$  collisions (panel (a)) and  $\pi^- + W$  (panel (b)) reactions, except for low rapidities in the latter reaction. On the other hand, SMASH underestimates the differential cross section almost over the entire  $p_T$  range for the lighter nucleus, while the shape agrees rather well. Also the

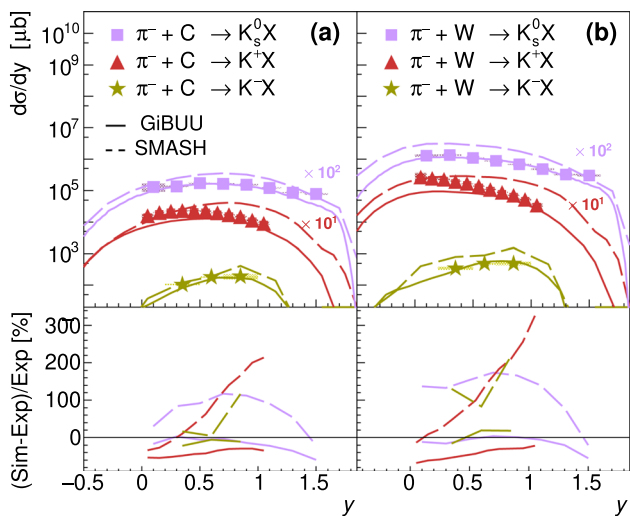


**Fig. 16** Comparison of the  $K_S^0$  (violet rectangles),  $K^+$  [30] (red triangles) and  $K^-$  [30] (green stars) cross sections as a function of rapidity with GiBUU (solid curves) and SMASH (long-dashed curves). The representation is analogous to Fig. 14

model results for the antikaon cross section as a function of rapidity is investigated in Fig. 16. GiBUU slightly underestimates the  $K^-$  production cross section off carbon, while the production cross section off tungsten is slightly overestimated. Both shapes are rather well reproduced by GiBUU. For the heavier nucleus, SMASH is able to reproduce the experimental data. Only minor deviations are observed for low rapidity. In general, the experimental data and GiBUU are almost consistent.

In summary, neither GiBUU nor SMASH can precisely describe simultaneously the cross sections as function of transverse momentum and rapidity in terms of shape and absolute yield of the presented comprehensive hadron set.

#### 4 (Semi-) Exclusive data analysis

At the pion beam momentum of 1.7 GeV/c, which is studied here, strangeness production occurs mainly in first-chance  $\pi^- + N$  collisions with a kaon and a  $\Lambda$  (or  $\Sigma$ ) in the final state. In addition, several other semi-inclusive channels contribute as well (see Table 4).

Although GiBUU describes the inclusive  $K_S^0$  data reasonably well, the agreement with inclusive  $\Lambda$  and  $K^+$  data is not satisfactory. Therefore, more information is gained by also analysing the (semi-)exclusive channel  $\pi^- + A \rightarrow \Lambda + K_S^0 + X$  for both colliding systems, allowing a comparison of the data on associated strangeness production to model calculations. The corresponding final states are reconstructed via the weak charged decays of the  $\Lambda$  and the  $K_S^0$  inside the HADES acceptance. The following final states are analysed:  $\Lambda + K_S^0$ ,  $\Lambda + K_S^0 + \pi^{0,-}$ ,  $\Sigma^0 + K_S^0$  and  $\Sigma^0 + K_S^0 + \pi^{0,-}$ . These

**Table 4** The production channels of  $\Lambda$  and  $K^0$  in elementary  $\pi^- N$  reactions together with the corresponding threshold momenta of the incident pions.

Channel	$p_{thr}$ [GeV/c]	$\sigma_{fit}$ [mb]	$\sigma_{GiBUU}$ [mb]	$\sigma_{SMASH}$ [mb]
$\Lambda K^0$	0.896	0.177	0.067	0.163
$\Sigma^0 K^0$	1.031	0.146	0.132	0.105
$\Sigma^- K^+$	1.035	0.150	0.156	0.130
$\Lambda \pi^0 K^0$	1.140	0.118	0.110	0.074
$\Lambda \pi^- K^+$	1.144	0.079	0.091	0.149
$\Sigma^+ \pi^- K^0$	1.290	0.014	0.015	0.005
$\Sigma^0 \pi^0 K^0$	1.286	0.034	0.030	0.136
$\Sigma^0 \pi^- K^+$	1.290	0.022	0.021	0.269
$\Sigma^- \pi^+ K^0$	1.305	0.037	0.030	0.201
$\Sigma^- \pi^0 K^+$	1.290	0.019	0.015	0.102
$p K^0 K^-$	1.290	0.007	0.011	0.003
$n K^+ K^-$	1.495	0.023	0.022	0.024
$n \phi$	1.559	0.027	0.020	–
$\Lambda \pi^+ \pi^- K^0$	1.423	0.003	–	–
$\Lambda \pi^0 \pi^- K^+$	1.407	0.002	–	–
$\Sigma^+ \pi^0 \pi^- K^0$	1.564	$\approx 0$	–	–
$\Sigma^+ \pi^- \pi^- K^+$	1.568	$\approx 0$	–	–
$\Sigma^0 \pi^- \pi^+ K^0$	1.580	$\approx 0$	–	–
$\Sigma^- \pi^+ \pi^0 K^0$	1.580	$\approx 0$	–	–
$\Sigma^- \pi^+ \pi^- K^+$	1.580	$\approx 0$	–	–
$\pi^- + n$				
$\Sigma^- K^0$	1.038	$< 0.049$	0.458	0.273
$\Sigma^- \pi^0 K^0$	1.296	$< 0.042$	0.036	0.505
$\Sigma^- \pi^- K^+$	1.290	$< 0.070$	0.025	1.035

The cross section  $\sigma_{fit}$  at  $p_{\pi^-} = 1.7$  GeV/c represents the value obtained from a fit according to the parametrisation given in [41, 42] to experimental data at several beam momenta. Also listed are  $\sigma_{GiBUU}$ , where the parametrisations were evaluated at the proper incident pion momenta, and  $\sigma_{SMASH}$ , where the cross sections were extracted in elementary mode. Channels not included in the models are labeled with “–”

include contributions from the production of  $\Sigma^- K_S^0$  with the subsequent strong conversion process of  $\Sigma^- N \rightarrow \Lambda (\Sigma^0) N$ .

##### 4.1 Event hypothesis and constraints

Considering the decay patterns of  $\Lambda \rightarrow p \pi^-$  and  $K_S^0 \rightarrow \pi^+ \pi^-$ , two positively and two negatively charged tracks are required as a minimal event selection criterion. Due to the limited acceptance for events with four charged particles in HADES, a different particle identification based on probability and event hypothesis is employed. All negatively charged particles are assumed to be  $\pi^-$  originating from strange particle decays, and an additional selection on the reconstructed mass, as calculated from the momentum and velocity measurement, of  $m_{\pi^-} > 80$  MeV/c<sup>2</sup> is applied. For

the remaining two positively charged particles, a likelihood method is employed, selecting the best matching candidate for a proton, based on the difference to the theoretical values of its velocity and energy loss  $dE/dx$  in the MDCs. In addition, the proton candidate had to fulfill a mass selection of  $800 < m_p$  [MeV/c<sup>2</sup>] < 1400. Finally, the remaining positively charged particle is accepted as a  $\pi^+$  if its mass fulfilled the condition of  $80 < m_{\pi^+}$  [MeV/c<sup>2</sup>] < 400. To resolve the ambiguity of the negative pion originating from the different sources, the possible combinations  $\Lambda_1(p, \pi_1^-)K_{S,1}^0(\pi^+\pi_2^-)$  and  $\Lambda_2(p, \pi_2^-)K_{S,2}^0(\pi^+\pi_1^-)$  are formed. Only the combination with the best matching of the invariant mass of  $p\pi^-$  pairs ( $M_{p\pi^-}$ ) to the nominal  $\Lambda$  mass and of the invariant mass of  $\pi^+\pi^-$  pairs ( $M_{\pi^+\pi^-}$ ) to the nominal  $K_S^0$  mass is considered for the further analysis. The plot of the corresponding correlations is shown in Fig. 17. This selection does not introduce any bias as the invariant masses of the rejected combination do not fit the  $\Lambda$  and  $K_S^0$  hypotheses.

The final data sample is selected using a two-dimensional elliptical (TDE) area around the invariant mass correlation with half-axes of  $\pm 3\sigma$ :

$$\sqrt{\left(\frac{\Delta M_{\Lambda} - \mu_{\Lambda}}{3 \cdot \sigma_{\Lambda}}\right)^2 + \left(\frac{\Delta M_{K_S^0} - \mu_{K_S^0}}{3 \cdot \sigma_{K_S^0}}\right)^2} \leq 1, \quad (1)$$

where  $\sigma_{\Lambda(K_S^0)}$  denotes the width,  $\mu_{\Lambda(K_S^0)}$  the offset and  $\Delta M_{\Lambda(K_S^0)}$  the difference of the invariant mass to the nominal mass. The width  $\sigma_{\Lambda}$  ( $\sigma_{K_S^0}$ ) is extracted by fitting the invariant-mass distribution  $M_{p\pi^-}$  ( $M_{\pi^+\pi^-}$ ), which has been pre-selected to be within a  $\pm 3\bar{\sigma}_{K_S^0}$  ( $\pm 3\bar{\sigma}_{\Lambda}$ ) window around the invariant mass  $M_{\pi^+\pi^-}$  ( $M_{p\pi^-}$ ) with  $\bar{\sigma}_{K_S^0}$  ( $\bar{\sigma}_{\Lambda}$ ) obtained beforehand in the inclusive analyses. The invariant mass distributions are modeled with a Gaussian for the signal and a second-order polynomial for the background. This choice ensures a minimal loss of signal, while obtaining a data sample with a signal-to-background ratio between  $S/B = 1.3$  and 5.45.

To reject the remaining background after the TDE selection, a sideband subtraction is employed. Since the selection of the semi-exclusive  $\Lambda K_S^0$  channel is based on the correlation of invariant mass spectra, a simple one-dimensional sideband is not applicable separately for each particle. To extract a suitable sample containing enough statistics to describe the background in the signal area, a TDE selection of  $4\sigma_{\Lambda(K_S^0)} - 15\sigma_{\Lambda(K_S^0)}$  is applied to the invariant mass correlation, indicated by the black ellipse in Fig. 17. This sideband sample thus accounts for the kinematic correlation of the  $\Lambda$  and  $K_S^0$ . For the sideband subtraction, the sideband sample has to be scaled to the background contribution after the TDE selection. The corresponding scaling factor is extracted in the following way. The total  $\Lambda$  and  $K_S^0$  signal is obtained by fitting both invariant mass distributions before the TDE selec-

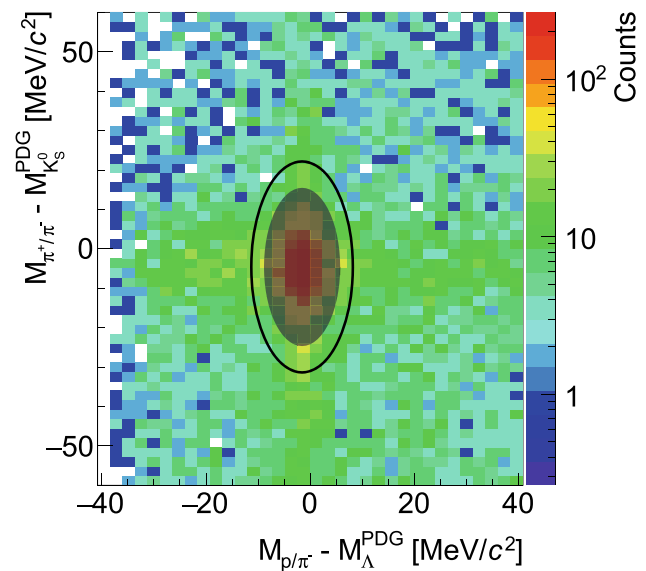


**Fig. 17** Yield distribution in the plane of the invariant mass of  $\pi^+\pi^-$  pairs vs the invariant mass of  $p\pi^-$  pairs, both subtracted by their nominal mother particle mass. The grey shaded area indicates the  $3\sigma$  TDE selection, while the black ellipse represents the lower boundary for the two-dimensional side-band, spanning from  $4\sigma - 15\sigma$ . A clear peak at the origin is visible, with a small background contribution

tion. Since, after the TDE selection, the total  $\Lambda$  and  $K_S^0$  signal stays the same, but the underlying background is altered and thus cannot be well described by any fitting procedure, the background contribution is estimated by subtracting the combined  $\Lambda$  and  $K_S^0$  signal from the total yield of invariant mass distributions. The sideband sample is scaled to the estimated background after the TDE selection and the obtained distribution is then subtracted from all spectra fulfilling the TDE selection. The kinematic distributions obtained after the subtraction are used for the kinematic investigations and comparisons performed later on. Figures 18 and 19 show the transverse momentum (Fig. 18a and Fig. 19a) and rapidity (Figs. 18b and 19b) distributions for  $K_S^0$  and  $\Lambda$  inside the HADES acceptance for the C target (purple circles) and the W target (orange stars) without any corrections for reconstruction efficiency. Therefore, the simulated kinematic distributions by GiBUU have been convoluted with the acceptance and efficiency of HADES to allow for a direct comparison.

## 4.2 Systematics

To estimate the systematic uncertainty introduced by the described analysis procedure all applied selections are varied and their impact on the final spectra is investigated. As the exclusive data is not corrected for efficiency and acceptance effects, the impact on the shape of the distribution and not on the yield is studied. In this way the whole analysis procedure is performed with another selection set and then compared

to the shape of the nominal selection set by calculating the difference in each point, after performing a  $\chi^2$  minimization.

In total eight different variations have been considered:  $\pm 1\sigma$  variation for the extraction of the particle invariant mass widths,  $\pm 0.5\sigma$  for the TDE selection,  $5 < \sigma_{\Lambda(K_S^0)} < 15$  and  $4 < \sigma_{\Lambda(K_S^0)} < 10$  for the sideband region, and the signal yield is taken solely from the  $K_S^0$  or  $\Lambda$ . The signal to background ratio for the carbon target for the nominal selection set is 2.4 and varies systematically from 1.8 to 5.0. For the tungsten target the corresponding value is 3.1 and the systematics is found to be in between 2.0 to 8.2. The same procedure is performed for the simulation, where the combined variations are smaller than the line width.

### 4.3 Comparison to transport models

In this analysis the spectra are simultaneously analyzed and fitted to the distribution from the transport calculation. A filtering of the transport calculation through the experimental response matrix is therefore the straight forward and more convenient approach.

As GiBUU allows to reconstruct the particle history we restrict the theory comparison to this model. Figures 18 and 19 show the transverse momentum and rapidity distributions for  $K_S^0$  and  $\Lambda$  inside the HADES acceptance for the C target (purple circles) and the W target (orange stars) compared to results from GiBUU. For this comparison we focus on the shape of the spectra, therefore the simulated distributions have been scaled to the experimental distributions by means of a global  $\chi^2/d.o.f.$  minimization procedure. The experimental  $p_T$  spectrum for the  $K_S^0$  in Fig. 18a for the heavy target is rather symmetric with a maximum around 300 MeV/c. GiBUU however predicts a distribution that is shifted to lower  $p_T$ , peaking at 200 MeV/c, with  $\chi^2/d.o.f. = 28.2$ . For the lighter target, the maximum of the experimental distribution is shifted to higher  $p_T$  around 400 MeV/c featuring an asymmetric shape, while GiBUU predicts a more symmetric shape, with a lower maximum and a lower selection-off of the distribution and a corresponding  $\chi^2/d.o.f. = 28.5$ . In both cases the experimental shape cannot be reproduced. The rapidity distribution of  $K_S^0$  (Fig. 18b) for the heavy system (W) is rather symmetric with a maximum at about 0.7 and a shift to lower rapidities with respect to the smaller colliding system. This is well reproduced by the GiBUU model as reflected by a  $\chi^2/d.o.f. = 1.8$  and points to  $K^0$  scattering inside the heavy nucleus, also seen in the inclusive spectra. In case of the lighter system (C), where the distribution is shifted to higher rapidities, GiBUU can reproduce the data qualitatively, with a slightly smaller maximum and a  $\chi^2/d.o.f.$  of 2.7.

The transverse momentum distributions of the  $\Lambda$  hyperons are shown in Fig. 19a. Both experimental distributions

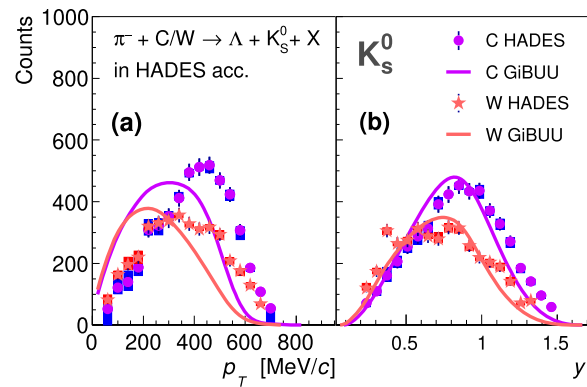


**Fig. 18** Transverse momentum and rapidity distributions of  $K_S^0$  in the (semi-)exclusive channel  $\pi^- + A \rightarrow \Lambda(\Sigma^0) + K_S^0 + X$  without reconstruction efficiency correction inside the HADES acceptance together with the GiBUU predictions. **a** Transverse momentum spectra of the  $K_S^0$  for the lighter carbon target (purple circles) and the heavier tungsten nuclei (orange stars). For the experimental data the statistical errors are indicated by error bars and systematic uncertainties indicated by shaded boxes, while the systematic uncertainties for the simulation are smaller than the width of the drawn line. **b** Rapidity distribution for the  $K_S^0$  with the same convention as for the transverse momentum

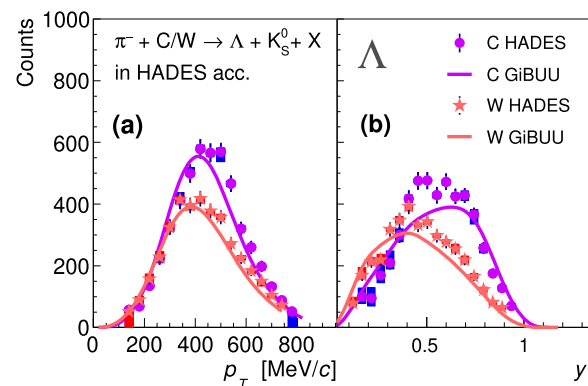


**Fig. 19** As Fig. 18 but for  $\Lambda$

have rather similar shapes, although in  $\pi^- + C$  reactions the distribution is shifted to higher  $p_T$ . In both cases GiBUU is able to reproduce the  $p_T$  dependence very well in the low  $p_T$  region, with a slight systematic shift towards the high  $p_T$  region and a corresponding  $\chi^2/d.o.f.$  of 2.7 and 1.8 for carbon and tungsten, respectively. The situation changes for the rapidity distributions. For the heavier target a maximum around 0.4 is observed. GiBUU can predict the shape qualitatively with  $\chi^2/d.o.f. = 2.8$ , while the deviations in the lighter system increase, as reflected in  $\chi^2/d.o.f. = 4.1$ . In general, the rapidity distributions of both particles in both nuclear systems are qualitatively reproduced, where again a backward shift is observed, pointing to scattering inside the heavy nucleus. In case of the transverse momentum distribution of  $K_S^0$ , the results of GiBUU show larger deviations while for the  $\Lambda$ s they are qualitatively reproduced. If one

considers the global  $\chi^2$ , the results for the heavier system are slightly better with a  $\chi^2$  of 9.38 compared to the lighter one with 10.26. Nevertheless, a satisfactory description of all kinematic observable simultaneously in both systems is not achieved, which is consistent with the results of, the inclusive analysis of strange hadrons above.

The (semi-) exclusive data might be the ideal tool to test the implementation of interaction potentials in transport models simultaneously for kaons and hyperons in the future, especially in light of the new constraints on these interactions extracted from femtoscopy measurements [43–45].

## 5 Summary and conclusion

We presented the inclusive differential cross sections as a function of transverse momentum  $p_T$  and rapidity  $y$  for  $\pi^+$ ,  $\pi^-$ ,  $p$ ,  $\Lambda$  and  $K_S^0$  measured in  $\pi^- + C$  and  $\pi^- + W$  reactions at an incident pion momentum of  $p_{\pi^-} = 1.7$  GeV/ $c$  within the rapidity range covered by the HADES detector. The presented data significantly extend the world data base on hadron production in pion-induced reactions on nuclear targets.

Scattering effects are observed, shifting the maximum of the  $\pi^+$ ,  $\pi^-$ ,  $\Lambda$  and  $K_S^0$  rapidity distributions to smaller rapidities in the heavier target.

The  $p_T$  and rapidity spectra have been compared to two state-of-the-art transport models, GiBUU and SMASH. To provide a more complete picture of the (strange) meson production, the published inclusive double-differential production cross section of  $K^\pm$  measured in the same systems [30], are compared with theory as well. In both transport models presented, no in-medium potentials for the  $KN$  or  $\Lambda N$  interactions are included.

Concerning the phase space distributions of  $\pi^+$  in  $\pi^- + C$  reactions, GiBUU describes (almost) the experimental data in terms of the shape and absolute cross section, whereas in  $\pi^- + W$  reactions the cross section is significantly overestimated with deviations up to factor of two. SMASH overestimates the experimental data in both colliding systems with deviations as large as a factor of three. Similar to the  $\pi^+$ , both models overestimate the  $\pi^-$  differential cross sections. Hence, the description of rescattering and/or absorption effects seems to be particularly insufficient, as the model calculations present larger deviations for the heavier target (W) and for the (quasi)-elastically scattered  $\pi^-$ . GiBUU is also not able to describe the (quasi)-elastically scattered protons. While the results of GiBUU for  $K_S^0$  and  $K^-$  are rather consistent with our data, the cross sections of  $\Lambda$  and  $K^+$  are under-estimated. In general, due to the imperfect description of all observable of the comprehensive hadron set ( $\pi^\pm$ ,  $\Lambda$ ,  $K_S^0$  and  $K^\pm$ ), an improvement of these models becomes desir-

able, especially with regard to the interpretation of heavy-ion data.

Furthermore, the phase-space distribution in the (semi-)exclusive channel  $\pi^- + A \rightarrow \Lambda + K_S^0 + X$  is investigated and a comparison to the GiBUU model is done. It is found that GiBUU cannot describe all the correlated kinematic observable simultaneously, in particular the calculation for the  $K_S^0$  transverse momentum distribution is not well reproduced.

**Acknowledgements** The HADES Collaboration thanks T Gaitanos, M. Bleicher, J. Steinheimer, H. Elfner, J. Staudenmaier and V. Steinberg for elucidating discussions. We gratefully acknowledge the support given by the following institutions and agencies: SIP JUC Cracow, Cracow (Poland), National Science Center, 2016/23/P/ST2/040 POLONEZ, 2017/25/N/ST2/00580, 2017/26/M/ST2/00600; WUT Warszawa (Poland) No: 2020/38/E/ST2/00019 (NCN), IDUB-POB-FWEiTE-3; TU Darmstadt, Darmstadt (Germany), DFG GRK 2128, DFG CRC-TR 211, BMBF:05P18RDFC1, HFHF, ELEMENTS: 500/10.006, VH-NG-823, GSI F&E, ExtreMe Matter Institute EMMI at GSI Darmstadt; Goethe-University, Frankfurt (Germany), BMBF: 05P12RFGHJ, GSI F&E, HIC for FAIR (LOEWE), ExtreMe Matter Institute EMMI at GSI Darmstadt; TU München, Garching (Germany), MLL München, DFG EClust 153, GSI TMLRG1316F, BmBF 05P15WOFCA, SFB 1258, DFG FAB898/2-2; JLU Giessen, Giessen (Germany), BMBF:05P12RGGHM; IJCLab Orsay, Orsay (France), CNRS/IN2P3, P2IO Labex, France; NPI CAS, Rez, Rez (Czech Republic), MSMT LM2018112, LTT17003, MSMT OP VVV CZ.02.1.01/0.0/0.0/18 046/0016066; IDUB-POB-FWEiTE-3. The following colleagues from Russian institutes did contribute to the results presented in this publication, but are not listed as authors following the decision of the HADES Collaboration Board on March 23, 2022: A. Belyaev, O. Fateev, M. Golubeva, F. Guber, A. Ierusalimov, A. Ivashkin, A. Kurepin, A. Kurilkin, P. Kurilkin, V. Ladygin, A. Lebedev, S. Morozov, O. Petukhov, A. Reshetin, A. Sadovsky.

**Funding** Open Access funding enabled and organized by Projekt DEAL. The publication is funded by the Open Access Publishing Fund of GSI Helmholtzzentrum fuer Schwerionenforschung.

**Data Availability Statement** Data will be made available on reasonable request. [Author's comment: Data will be made available on HEP-data soon.]

**Code Availability Statement** This manuscript has no associated code/software [Author's comment: Code/software will be made available on reasonable request.]

**Open Access** This article is licensed under a Creative Commons Attribution 4.0 International License, which permits use, sharing, adaptation, distribution and reproduction in any medium or format, as long as you give appropriate credit to the original author(s) and the source, provide a link to the Creative Commons licence, and indicate if changes were made. The images or other third party material in this article are included in the article's Creative Commons licence, unless indicated otherwise in a credit line to the material. If material is not included in the article's Creative Commons licence and your intended use is not permitted by statutory regulation or exceeds the permitted use, you will need to obtain permission directly from the copyright holder. To view a copy of this licence, visit <http://creativecommons.org/licenses/by/4.0/>.

## References

1. R. Brockmann, W. Weise, Phys. Lett. B **367**, 40 (1996)
2. G.E. Brown, M. Rho, Phys. Rev. Lett. **66**, 2720 (1991)
3. T. Hatsuda, S.H. Lee, Phys. Rev. C **46**, R34 (1992)
4. V. Bernard and U. G. Meissner, Nucl. Phys. A **489** (1988)
5. R. Rapp, J. Wambach, Adv. Nucl. Phys. **25**, 1 (2000)
6. B. Friman, C. Hohné, J. Knoll, S. Leupold, J. Randrup, R. Rapp, P. Senger, Lect. Notes Phys. **814**, 11 (2011)
7. D. Lonardoní, A. Lovato, S. Gandolfi, F. Pederiva, Phys. Rev. Lett. **114**, 092301 (2015). <https://doi.org/10.1103/PhysRevLett.114.092301>
8. H. Djapo, B.-J. Schaefer, J. Wambach, Phys. Rev. C **81**, 035803 (2010). <https://doi.org/10.1103/PhysRevC.81.035803>
9. J. Schaffner-Bielich, Nucl. Phys. A **835**, 279 (2010). <https://doi.org/10.1016/j.nuclphysa.2010.01.203>
10. S. Petschauer, J. Haidenbauer, N. Kaiser, U.-G. Meißner, W. Weise, Eur. Phys. J. A **52**, 15 (2016). <https://doi.org/10.1140/epja/i2016-16015-4>
11. S. Leupold, V. Metag, U. Mosel, Int. J. Mod. Phys. E **19**, 147 (2010)
12. R.S. Hayano, T. Hatsuda, Rev. Mod. Phys. **82**, 2949 (2010)
13. G. Agakishiev et al., Eur. Phys. J. A **50**, 82 (2014). <https://doi.org/10.1140/epja/i2014-14082-1>
14. J. Adamczewski-Musch et al., HADES. Phys. Rev. C **95**, 065205 (2017). <https://doi.org/10.1103/PhysRevC.95.065205>
15. G. Agakishiev et al., (HADES). Eur. Phys. J. A **51**, 137 (2015). <https://doi.org/10.1140/epja/i2015-15137-5>
16. C. Hartnack, H. Oeschler, Y. Leifels, E.L. Bratkovskaya, J. Aichelin, Phys. Rep. **510**, 119 (2012). <https://doi.org/10.1016/j.physrep.2011.08.004>
17. W. Reisdorf et al., (FOPI). Nucl. Phys. A **781**, 459 (2007). <https://doi.org/10.1016/j.nuclphysa.2006.10.085>
18. C. Fuchs, Prog. Part. Nucl. Phys. **56**, 1 (2006). <https://doi.org/10.1016/j.pnpnp.2005.07.004>
19. A. Förster, (KaoS). J. Phys. G **28**, 2011 (2002). <https://doi.org/10.1088/0954-3889/28/7/363>
20. V. Zinyuk et al., FOPI. Phys. Rev. C **90**, 025210 (2014). <https://doi.org/10.1103/PhysRevC.90.025210>
21. G. Agakishiev et al., HADES. Phys. Rev. C **90**, 054906 (2014). <https://doi.org/10.1103/PhysRevC.90.054906>
22. G. Agakishiev et al., HADES. Phys. Rev. C **82**, 044907 (2010). <https://doi.org/10.1103/PhysRevC.82.044907>
23. P. Salabura, J. Stroth, Prog. Part. Nucl. Phys. **120**, 103869 (2021). <https://doi.org/10.1016/j.pnpnp.2021.103869>
24. M. Benabderrahmane et al., FOPI. Phys. Rev. Lett. **102**, 182501 (2009). <https://doi.org/10.1103/PhysRevLett.102.182501>
25. M. Buescher et al., Eur. Phys. J. A **22**, 301 (2004). <https://doi.org/10.1140/epja/i2004-10036-6>. arXiv:nucl-ex/0401031
26. O. Buss, T. Gaitanos, K. Gallmeister, H. van Hees, M. Kaskulov, O. Lalakulich, A. Larionov, T. Leitner, J. Weil, U. Mosel, Phys. Rep. **512**, 1 (2012). <https://doi.org/10.1016/j.physrep.2011.12.001>
27. J. Weil et al., Phys. Rev. C **94**, 054905 (2016). <https://doi.org/10.1103/PhysRevC.94.054905>
28. G. Agakishiev et al., HADES. EPJ **A41**, 243 (2009). <https://doi.org/10.1140/epja/i2009-10807-5>
29. J. Adamczewski-Musch et al., HADES. Eur. Phys. J. A **53**, 188 (2017). <https://doi.org/10.1140/epja/i2017-12365-7>
30. J. Adamczewski-Musch et al., HADES. Phys. Rev. Lett. **123**, 022002 (2019). <https://doi.org/10.1103/PhysRevLett.123.022002>
31. S. Maurus, PhD Thesis, TUM (2019)
32. J. Wirth, PhD Thesis, TUM (2019)
33. C. Patrignani et al., Chin. Phys. C **40**, 100001 (2016). <https://doi.org/10.1088/1674-1137/40/10/100001>
34. J. Adamczewski-Musch et al., (HADES). Phys. Rev. C **102**, 024001 (2020). <https://doi.org/10.1103/PhysRevC.102.024001>
35. J. Adamczewski-Musch et al. (HADES), (2022) arXiv:2202.12750 [nucl-ex]
36. I. Fröhlich et al., PoS **ACAT**, 076 (2007), <https://doi.org/10.22323/1.050.0076> arXiv:0708.2382 [nucl-ex]
37. Y.-X. Zhang et al., TMEP. Phys. Rev. C **97**, 034625 (2018). <https://doi.org/10.1103/PhysRevC.97.034625>. arXiv:1711.05950 [nucl-th]
38. A. Ono et al., TMEP. Phys. Rev. C **100**, 044617 (2019). <https://doi.org/10.1103/PhysRevC.100.044617>. arXiv:1904.02888 [nucl-th]
39. M. Colonna et al., TMEP. Phys. Rev. C **104**, 024603 (2021). <https://doi.org/10.1103/PhysRevC.104.024603>. arXiv:2106.12287 [nucl-th]
40. D. Cabrera, L. Tolós, J. Aichelin, E. Bratkovskaya, Phys. Rev. C **90**, 055207 (2014). <https://doi.org/10.1103/PhysRevC.90.055207>
41. A.A. Sibirtsev, W. Cassing, C.M. Ko, Z. Phys. A **358**, 101 (1997). <https://doi.org/10.1007/s002180050282>
42. W. Cassing, E.L. Bratkovskaya, U. Mosel, S. Teis, A. Sibirtsev, Nucl. Phys. A **614**, 415 (1997). [https://doi.org/10.1016/S0375-9474\(96\)00461-7](https://doi.org/10.1016/S0375-9474(96)00461-7)
43. J. Adamczewski-Musch et al., HADES. Phys. Rev. C **95**, 015207 (2017). <https://doi.org/10.1103/PhysRevC.95.015207>
44. S. Acharya et al., ALICE. Phys. Rev. C **99**, 024001 (2019). <https://doi.org/10.1103/PhysRevC.99.024001>
45. S. Acharya et al., ALICE. Phys. Lett. B **805**, 135419 (2020)